Journal of Power Sources 196 (2011) 3955–3961

Contents lists available at ScienceDirect

Journal of Power Sources

journal homepage: www.elsevier.com/locate/jpowsour

First-principles modelling of lithium iron oxides as battery cathode materials

Michele Catti*, Merced Montero-Campillo

Dipartimento di Scienza dei Materiali, Università di Milano Bicocca, via Cozzi 53, 20125 Milano, Italy

ARTICLE INFO

Article history:
Received 20 September 2010
Received in revised form 25 October 2010
Accepted 7 November 2010
Available online 16 November 2010

Keywords:
First-principles calculations
Lithium iron oxides
Theoretical charge/discharge energy

ABSTRACT

Starting from published charge/discharge curves and X-ray data on *Pmmn*-$LiFeO_2$ and $LiFe_5O_8$ as cathode materials vs. Li anode, a scheme of electrochemical reactions is proposed to explain the unclear electrode functionality of the 'corrugated layer' $LiFeO_2$ phase. The scheme was validated by quantum-mechanical calculations (CRYSTAL09 code, hybrid B3LYP Hamiltonian) on a number of structural models for $Li_{1-x}FeO_2$, $LiFe_5O_8$, and $Li_3Fe_5O_8$. Magnetic interactions were taken into account, finding antiferromagnetic ($Li_{1-x}FeO_2$) and ferrimagnetic ($LiFe_5O_8$ and $Li_3Fe_5O_8$) orderings as stable states. At variance with spinel-like $LiFe_5O_8$, $Li_3Fe_5O_8$ displays a rocksalt-type superstructure. The computed energies for reactions (I) $4LiFeO_2 \rightarrow 4Li_{0.75}FeO_2 + Li$, (II) $4Li_{0.75}FeO_2 + Li \rightarrow 4/5LiFe_5O_8 + 8/5Li_2O$, and (III) $1/2LiFe_5O_8 + Li \leftrightarrow 1/2Li_3Fe_5O_8$ are 4.44, −3.62, and −2.10 eV, respectively. Such values compare satisfactorily with the average charge/discharge voltages observed for positive electrodes made up of *Pmmn*-$LiFeO_2$ and of $LiFe_5O_8$.

1. Introduction

In most rechargeable Li-ion batteries of commercial use, the cathode is made by lithium cobalt oxide against an anode of graphite. This actually works satisfactorily, but two inconveniences are well known: cobalt is toxic and expensive, so as to raise problems with the disposal of exhausted devices and with their production cost. Many alternative cathode materials have been searched for in the last two decades [1,2]. Those based on lithium iron oxides are particularly attractive, because of the low cost and absence of toxicity of iron. The simplest compound of this family is $LiFeO_2$, which indeed shows a quite complex polymorphism.

At least nine phases of $LiFeO_2$ are reported in the literature [3]. The first group is formed by the cubic disordered rocksalt-type α phase, and by its β (tetragonal), β′ (monoclinic), and γ (tetragonal) superstructures [4,5]. Then a rhombohedral ordered rocksalt superstructure analogous to $LiCoO_2$ ('layer structure') [6], a hollandite-type tetragonal phase [7], and three orthorhombic phases isostructural with $LiMnO_2$ [8], with β-$NaFeO_2$ [9], and with ramsdellite [10] were described. Yet complete structure determinations of many of these phases are missing. Most of these polymorphs were tested as electrode materials against a lithium metal anode. The claimed performances are variable: some phases seem not to work (β′ and γ), and for others there are often contradictory reports. Favourable results are given for the α [11–13], β-$NaFeO_2$-type [9] and ramsdellite-type [10,14] modifications. The best reports seem to be those concerning the so called 'corrugated layer' polymorph, with orthorhombic *Pmmn* structure isomorphous to that of the corresponding phase of $LiMnO_2$ (Fig. 1).

Charge–discharge curves of a *Pmmn*-$LiFeO_2$ cathode against Li anode were determined by several authors [8,10,14–17]. In all cases, the first charge cycle shows a wide voltage plateau at about 4.2 V, suggesting a two-phase character of the electrode material during the first Li extraction cycle. Then the following charge–discharge cycles take a more regular aspect, with the voltage changing in the 1.5–3.5 range with good reversibility. The reported capacity varies from about 100 mA h g^{-1} (0.3 ÷ 0.4 e f.u.$^{-1}$) [8] to nearly 140 mA h g^{-1} (0.5 e f.u.$^{-1}$) [17]. Different interpretations are given, however, on the basis of XRPD data collected on the electrode material. In the earlier paper (ex-situ measurements), an amorphization process of the cathode during the first charge was suggested [8]. On the other hand, in situ data [17] would indicate the formation of spinel-like $LiFe_5O_8$ in the first discharge cycle. This interpretation is also supported by magnetic measurements, showing the appearance of a spontaneous magnetic moment in the first discharge, consistent with the ferrimagnetic character of $LiFe_5O_8$ [17]. Further, electrochemical results on $LiFe_5O_8$ demonstrated its ability to intercalate/deintercalate up to two Li atoms f.u.$^{-1}$ reversibly [18,19]. By analysis of the XRPD intensities collected after discharge [18], the formed $Li_3Fe_5O_8$ phase was shown to have a rocksalt-type disordered structure, with the same lattice as spinel but with a different cation distribution. This feature could not appear in the corresponding electron diffraction pattern [19].

* Corresponding author. Tel.: +39 02 64485139; fax: +39 02 64485400.
E-mail address: catti@mater.unimib.it (M. Catti).

0378-7753/$ – see front matter © 2010 Elsevier B.V. All rights reserved.
doi:10.1016/j.jpowsour.2010.11.062

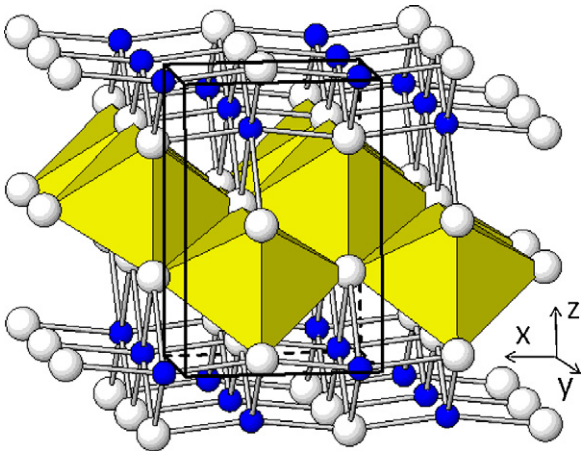

Fig. 1. Crystal structure of *Pmmn*-$LiFeO_2$ [8]. The FeO_6 coordination octahedra and the lithium corrugated layers are emphasized. Li and O atoms are dark grey (blue in the web version of this article) and white balls, respectively.

On the basis of the latter experimental data, we propose the following three-step scheme of electrochemical reactions to explain the functionality of the corrugated layer $LiFeO_2$ cathode.

- First charge: ~4.2 V

$$(1/x)LiFeO_2 \rightarrow (1/x)Li_{1-x}FeO_2 + Li \quad (I)$$

An $x < 1/2$ fraction of Li is extracted from lithium iron oxide, with partial oxidation of iron and formation of vacancies in the *Pmmn*-$LiFeO_2$ structure.

- First discharge: 4–2 V

$$(1/x)Li_{1-x}FeO_2 + Li \rightarrow (1/5x)LiFe_5O_8 + (2/5x)Li_2O \quad (II)$$

Instead of reinserting lithium, the Li-poor iron oxide reacts with lithium metal decomposing into the spinel-like phase plus lithium oxide, with reduction of Fe to the original +3 state. Li_2O is assumed to remain in the cathode as electrochemically inert phase, without taking part in the following reactions. Its presence would be hard to detect in the X-ray pattern, because of peak overlap and poor scattering power of Li.

- Subsequent discharge/charge cycles: 3.5–1.5 V

$$(1/2)LiFe_5O_8 + Li \leftrightarrow (1/2)Li_3Fe_5O_8 \quad (III)$$

Lithium is intercalated/deintercalated in and out of the structure of $LiFe_5O_8$, with the oxidation state of iron switching between +3 and +2.6.

Indeed, a final short plateau at about 4.5 V is also observed at the end of the charge cycles [17]. Although this feature resembles the long continuous plateau in the first charge, which was ascribed to reaction (I), delithiation extends here well beyond the previous capacity range. Further, diffraction and magnetic results [17] do not support the presence of $LiFeO_2$ in the electrode after cycling, so that a repeat of reaction (I) is not likely. Oxidation of $LiFe_5O_8$ to some partially delithiated $Li_{1-x}Fe_5O_8$ species would be probably responsible for this secondary feature, and also for the similar charging to 4.5 V reported for $LiFe_5O_8$ itself [19]. However, this process will not be further considered in the present work.

In order to validate the above three-step scheme, and thus to explain the behaviour of *Pmmn*-$LiFeO_2$ as cathode material on a sound basis, a first-principles quantum-mechanical study of reactions (I)–(III) and of all phases involved was undertaken. Theoretical tools proved to be quite effective at modelling several electrochemical systems [20–24], thus giving an important contribution to their understanding at an atomistic level. In view of the complexity of the present case, free energy changes will be approximated by energy changes: an estimate of configurational entropy by the ideal solution model shows that its contribution is comparatively small at room temperature, as discussed in the following sections. The main emphasis is on developing suitable structural models for defective $Li_{1-x}FeO_2$ and for $Li_3Fe_5O_8$, accounting also for magnetic ordering which gives a substantial energy contribution to these systems. The final aim is to compute the reactions energies and the corresponding average electrochemical potentials, to be compared with the experimental charge/discharge voltages.

2. Computational method

Quantum-mechanical calculations of the ground-state total crystal energy were performed by the computer code CRYSTAL09 [25], based on the periodic LCAO (Linear Combination of Atomic Orbitals) approach. A hybrid B3LYP functional, i.e., a balanced mixture of the DFT (Density-Functional-Theory)-LYP non-local correlation [26] with the DFT Becke's [27] and the Hartree–Fock exchange, was employed. All-electron basis sets of Gaussian-type functions were adopted for the radial parts of atomic orbitals, according to the schemes 8(*s*)64111(*sp*)411(*d*)G, 8(*s*)411(*sp*)1(*d*)G, and 5(*s*)11(*sp*)G for Fe, O and Li atoms, respectively, in all oxide phases. For Li metal, the richer 5(*s*)111(*sp*)G basis set was employed. The SCF (Self-Consistent-Field) equations were solved in spin-polarized form, so as to account for magnetic ordering.

The reciprocal space was sampled according to a regular sublattice of volume about 2×10^{-4} Å^{-3} per point. For instance, in the case of *Pmmn*-$LiFeO_2$ ($a = 4.061$, $b = 2.962$ and $c = 6.032$ Å from experiment [8]) the Monkhorst grid was defined by 4, 6, and 3 points along the three reciprocal axes, in order to achieve that point density. The five tolerances related to cut-off limits for series summation were set to 10^{-7}, 10^{-7}, 10^{-7}, 10^{-7}, and 10^{-14}. Convergence was also controlled by an ΔE threshold of 10^{-9} hartree per primitive unit cell in the SCF cycles. The integration of the DFT functionals was performed by use of the LGRID accuracy conditions. In order to accelerate the SCF convergence, the technique of level shifter was used, enhancing the energy difference between highest occupied and lowest empty states in the first cycles. Atomic coordinates and unit-cell constants were always optimized together by calculation of analytical gradients and subsequent conjugate gradients algorithm (FULLOPTG option).

The free energy changes were approximated by energy changes at 0 K. Thermal and configurational entropy effects were neglected. However, an estimate of configurational entropy according to the ideal solution model shows that, for reaction (I), at room temperature $-T\Delta_r S = -0.058$ and -0.096 eV for $x = 1/4$ and $1/16$, respectively. Such values are less than 2% of the corresponding $\Delta_r E$ results (Table 1).

3. Results and discussion

3.1. Vacancy patterns in $Li_{1-x}FeO_2$ and reaction (I)

In order to do calculations for the first reaction, we need structural models of the Li-deficient $Li_{1-x}FeO_2$ phase. By employing supercells of the basic stoichiometric structure (Fig. 1), a number of models were built up for each of the compositions $x = 1/4$, $1/8$, $1/12$, $1/16$. For each of them, the structure was optimized by full relaxation obtaining the corresponding total energy (Table 1). The local structural distortions in the vacancy neighbourhood can be clearly seen in Fig. 2, for three of the four vacancy compositions. However, the changes of lattice parameters are comparatively small with respect to pure *Pmmn*-$LiFeO_2$. The simpler ferromagnetic (FM) ordering was assumed in all cases, and the antiferromagnetic (AFM)

Table 1
Computed energies and lattice constants of the least-energy structural models of $Li_{1-x}FeO_2$ for different vacancy fractions *x*. Percent deviations from the experimental cell edges of *Pmmn*-$LiFeO_2$ [8] are given in parentheses. Ferromagnetic (FM) and antiferromagnetic (AFM) ordering is indicated. *Z* is the number of formula units (f.u.) per unit-cell, and $\Delta_r E$ refers to reaction (I).

	x				
	0	1/16	1/12	1/8	1/4
FM supercell	$a_0 \times b_0 \times c_0$	$2a_0 \times 4b_0 \times c_0$	$2a_0 \times 3b_0 \times c_0$	$2a_0 \times 2b_0 \times c_0$	$2a_0 \times 2b_0 \times c_0$
Space group	*Pmmn*	*Pmm*2	*Pmm*2	*Pmm*2	*Cmm*2
Z	2	16	12	8	8
a (Å)	4.101 (+1.0%)	8.214	8.219	8.237	8.291
b	2.975 (+0.4%)	11.886	8.895	5.916	5.882
c	6.124 (+1.5%)	6.139	6.143	6.132	6.143
$E + 1419$ (hartree f.u.$^{-1}$)	−2.79436	−2.31278	−2.15224	−1.83316	−0.87257
$\Delta_r E$ (eV)		4.825	4.830	4.399	4.332
$\Delta(x)$ (eV)		0	0.005	−0.426	−0.493
AFM supercell	$2a_0 \times b_0 \times c_0$				$2a_0 \times 2b_0 \times c_0$
S.G.	$P2_1/m$				*Pm*
Z	4				8
a (Å)	8.104				8.163
b	2.982				5.876
c	6.163				6.233
β (deg)	90.21				89.97
$E + 1419$ (hartree f.u.$^{-1}$)	−2.79730				−0.87453
$\Delta_r E$ (eV)					4.439
E (AFM) − E (FM) (eV f.u.$^{-1}$)	−0.080				−0.053

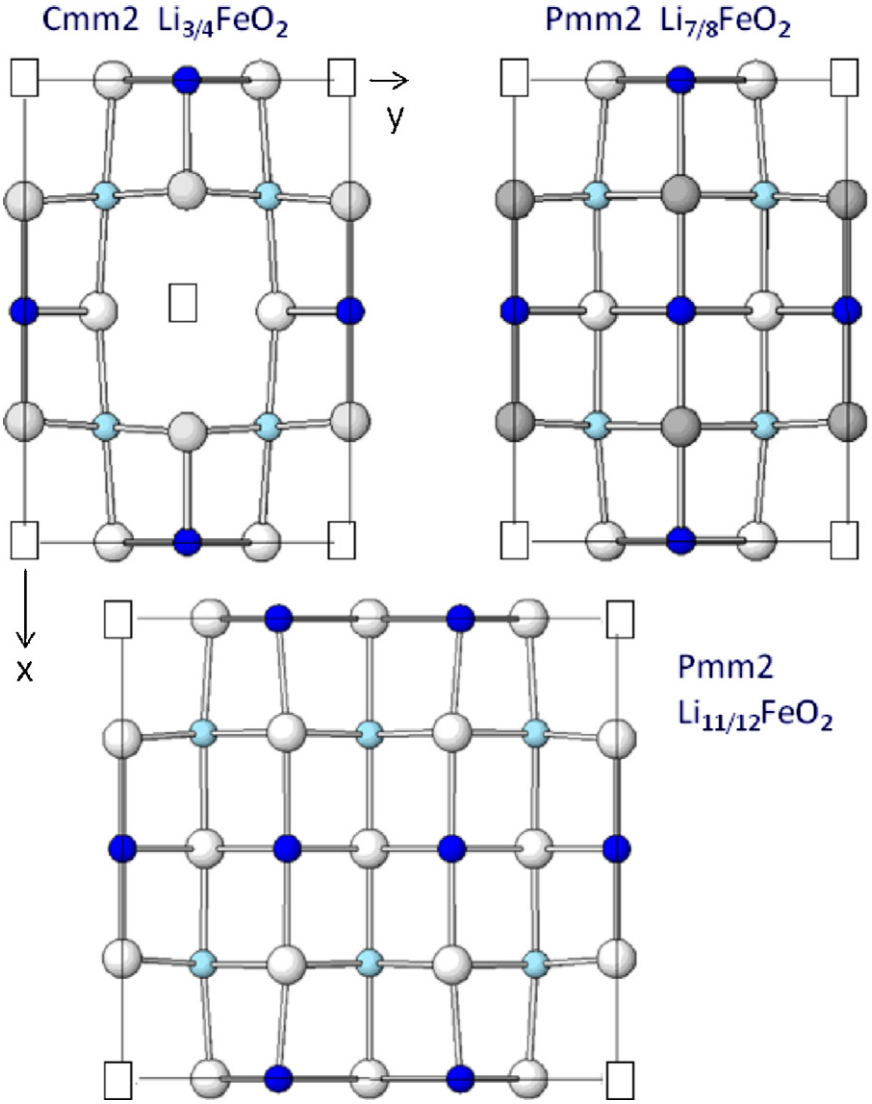

Fig. 2. Lithium vacancy (□) arrangements in the (0 0 1) corrugated layers of the least-energy optimized structures, for three compositions ($x = 1/4$, 1/8, and 1/12) of $Li_{1-x}FeO_2$.

one was considered only for the two compositional end-members. We shall discuss first the FM results, where the relevant physics of the system is already accounted for.

The most significant quantity reported in Table 1 is:

$$\Delta_r E(x) = (1/x)[E(Li_{1-x}FeO_2) - E(LiFeO_2)] + E(Li) = (1/x)\Delta E + E(Li)$$

This is the reaction (I) energy, i.e. the energy necessary to extract Li atoms with x density from the *Pmmn*-$LiFeO_2$ structure, and to insert them into BCC lithium metal, per Li atom. It also corresponds to the formation energy of a Li vacancy with density x in *Pmmn*-$LiFeO_2$, assuming as energy zero that of lithium metal. The calculated value of E(Li) was -7.527956 hartree atom^{-1}, with $a = 3.420$ Å as optimized cell edge. By normalizing reaction (I) to one Li atom one electron is exchanged in the Redox process, so that the $\Delta_r E$ value measured in eV is numerically equal to the opposite of the electrochemical potential E measured in Volts.

The dependence of $\Delta_r E$ on x indicates the effect of vacancy–vacancy interactions on their formation energy. The structural configurations of the two diluted vacancy cases ($x = 1/16$ and $1/12$) approximate the isolated vacancy situation (cf. Fig. 2), where interactions are absent. The corresponding 4.83 eV value can thus be considered as an estimate of the ideal single vacancy formation energy. Deviations from this value, expressed as $\Delta(x)$ in Table 1, are a measure of vacancy–vacancy interactions. Both vacancy-richer compositions ($x = 1/8$ and $1/4$) show negative values of -0.4 to -0.5 eV, indicating a stabilization interaction. This is due to the peculiar arrangement of [0 1 0] rows of alternating Li atoms and vacancies, which is observed in both cases (Fig. 2). It thus appears that a pair of vacancies in a [0 1 0] row is more stable when separated by a single Li atom, than by two or more of them. This was confirmed by building up structural models of the vacancy-rich compositions where such an arrangement was absent, and their energies proved to be similar to those of the vacancy-poor cases. For instance, for $x = 1/8$ a *Cmm*2 model with $2a_0 \times 4b_0 \times c_0$ supercell has vacancies separated by three Li atoms along the row: the computed energy was 4.95 eV, with a slight positive deviation with respect to isolated vacancies. On the other hand, the configuration with two adjacent vacancies along the row gave a large destabilization ($x = 1/4$, *Pmm*2 $a_0 \times 4b_0 \times c_0$ supercell, $\Delta_r E = 5.23$ eV). We can then conclude that, for phases with large vacancy density ($x > 0.1$), the [0 1 0] Li–□–Li–□–Li arrangement should be present and the vacancy formation energy $\Delta_r E$ should be similar to the 4.33 eV value obtained for $x = 0.25$.

Because of the two-phase character of the first charge curve obtained in the experimental electrochemical cell, a composition discontinuity can be assumed between stoichiometric *Pmmn*-$LiFeO_2$ and the $Li_{1-x}FeO_2$ phase with the largest Li deficiency ($x \geq 0.25$). Therefore, the corresponding reaction energy of 4.33 eV is the appropriate constant value for the whole x range. This energy compares quite well with the experimental 4.2 V voltage of the plateau observed in the first charge cycle.

Pmmn-$LiFeO_2$ is reported to be antiferromagnetic from 0 K to room temperature, on the basis of incomplete magnetic data [8,17]. Then the simplest AFM ordering scheme was adopted for the $LiFeO_2$ structure: the a_0 unit-cell edge was doubled, so as to alternate $Fe^{3+}\uparrow$ and $Fe^{3+}\downarrow$ ions along the [1 0 0] rows of corner-sharing FeO_6 octahedra, where Fe↑–O–Fe↓ superexchange interactions can take place. The same scheme holds for $Li_{0.75}FeO_2$, too. As expected, stabilization with respect to the FM arrangement is observed for both cases (Table 1); however, the effect is smaller for the Li-deficient composition. This means that superexchange is perturbed somehow by Li vacancies. As a result, the reaction energy increases slightly from 4.33 to 4.44 eV; this value should be the preferred one, as it is based on the most stable magnetic configurations

Table 2
Splitting of Wyckoff sites of the spinel structure with symmetry lowering down to orthorhombic $C222_1$.

Space group	$Fd\bar{3}m \rightarrow P4_332$	
Octahedral sites	16*d*	$12d_1 + 4b$
	16*c*	$12d_2 + 4a$
Tetrahedral sites	8*a*	$8c_a$
	8*b*	$8c_b$
Space group	$P4_332 \rightarrow C222_1$	
Octahedral sites	$12d_1$	$8c_1 + 8c_2 + 4a_1 + 4b_1$
	4*b*	$4a_2 + 4b_2$
	$12d_2$	$8c_3 + 8c_4 + 4a_3 + 4b_3$
	4*a*	$4a_4 + 4b_4$
Tetrahedral sites	$8c_a$	$8c_5 + 8c_6$

3.2. Magnetic structures of $LiFe_5O_8$ and $Li_3Fe_5O_8$

The crystal structure of $LiFe_5O_8$ (space group $P4_332$) is an ordered version of inverse spinel ($Fd\bar{3}m$), with Li and 3/5 of Fe atoms in octahedral sites, and 2/5 of Fe atoms in tetrahedral sites (Table 2) [28]. Magnetic measurements indicate that this compound is ferrimagnetic (FFM) at room temperature [29–31]: the net magnetic moment arises then from the difference between octahedral Fe^{3+} ions with majority spin and tetrahedral Fe^{3+} ions with minority spin (Fig. 3). Thus, a study of the magnetic structure of $LiFe_5O_8$ should be included in the modelling to insure appropriate energy results. Both the FM and FFM magnetic orderings are compatible with the $P4_332$ space group, but any antiferromagnetic arrangement of the spins requires that the symmetry is lowered to a subgroup of $P4_332$. The simplest AFM model can be built up within the $C222_1$ symmetry with a $\sqrt{2}a_0 \times \sqrt{2}a_0 \times a_0$ conventional cell (Table 2); with respect to the FFM case, 1/6 of the octahedral Fe^{3+} ions move from majority to minority spin, so as to make the net magnetic moment vanish.

In Table 3, the ideal fractional coordinates of the $C222_1$ structure are reported, with the site occupation pattern of AFM-$LiFe_5O_8$. The site patterns of all three magnetic structures (FM, FFM and AFM) considered for $LiFe_5O_8$, in the corresponding space groups, are given in Table 4. Therein also the results of the least-energy structure optimizations appear for each phase. Very strong ΔE stabilization energies are observed for both the FFM and AFM orderings with respect to the FM configuration; the values are about three times that computed for AFM-$LiFeO_2$ (cf. Table 1). However,

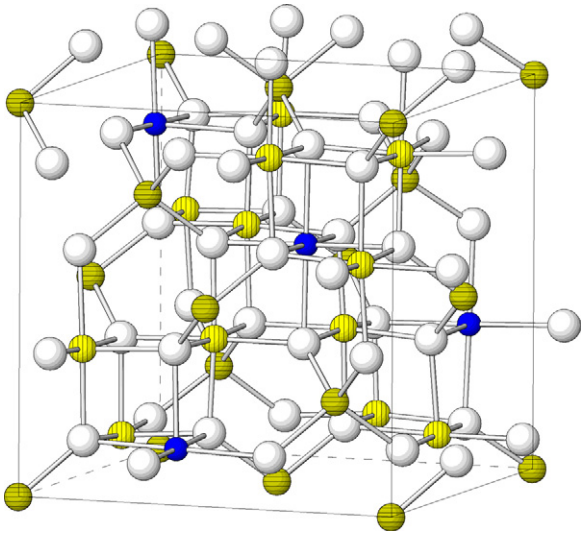

Fig. 3. Picture of the ferrimagnetic (cubic $P4_332$) structure of $LiFe_5O_8$. Li and O atoms are denoted as dark grey (blue in the web version) and white balls, respectively. Fe atoms are vertically- (majority spin) and horizontally- (minority spin) hatched spheres.

Table 3
Ideal fractional coordinates of the sites of space group $C222_1$ occupied by Fe and Li atoms in $LiFe_5O_8$ and $Li_3Fe_5O_8$. All sites are octahedral but those denoted by asterisks (tetrahedral). Antiferromagnetic (AFM) and ferromagnetic (FFM) orderings are specified.

Site	x	y	z	AFM-$LiFe_5O_8$	FFM-$Li_3Fe_5O_8$
$8c_1$	1/4	1/8	1/4	Fe↑	Fe↑
$8c_2$	3/8	1/4	0	Fe↑	Fe↑
$8c_3$	1/8	1/4	0		Li
$8c_4$	1/4	3/8	1/4		Fe↓
$8c_5$*	7/8	7/8	3/8	Fe↓	
$8c_6$*	5/8	1/8	7/8	Fe↓	
$4a_1$	7/8	0	0	Fe↑	Fe↑
$4b_1$	1/2	1/8	1/4	Fe↓	Fe↑
$4a_2$	3/8	0	0	Li	Li
$4b_2$	0	1/8	1/4	Li	Li
$4a_3$	5/8	0	0		Fe↓
$4b_3$	0	3/8	1/4		Li
$4a_4$	1/8	0	0		Fe↓
$4b_4$	1/2	3/8	1/4		Li

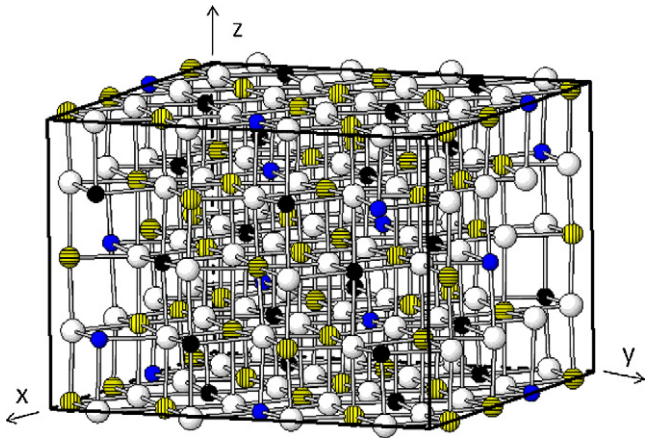

Fig. 4. Ordered (orthorhombic $C222_1$) ferrimagnetic structural model of $Li_3Fe_5O_8$. Black balls indicate additional intercalated Li atoms with respect to $LiFe_5O_8$.

the FFM result is significantly larger in modulus (−0.262 against −0.212 eV Fe atom^{-1}) than the AFM one, confirming that the stable structure of $LiFe_5O_8$ is ferrimagnetic as shown by experiment. The calculated volume of the FFM phase also shows the best agreement with the experimental value [18] (+3.7% deviation), whereas for the other phases larger positive deviations are observed.

In order to accommodate additional Li atoms into the spinel-like $LiFe_5O_8$ structure, the 4*a* and $12d_2$ empty octahedral sites cannot be utilized, because they are too close to Fe↓ atoms in the tetrahedral $8c_a$ position. Similarly, the empty tetrahedral $8c_b$ site is useless because near to Fe↑ in $12d_1$ e to Li in 4*b*. Therefore, Fe↓ atoms must be moved from the tetrahedral $8c_a$ site into an octahedral one, so as to insert additional lithium into the other empty octahedral positions. The structure obtained has thus all metal atoms in octahedral sites, with the tetrahedral ones empty: it is no more a spinel, but a rocksalt-type superstructure. For the $Li_3Fe_5O_8$ composition, the only possible arrangement within the original $P4_332$ space group is Fe in $12d_1$, 4*a* and 4*b*, and Li in $12d_2$. Unfortunately, this arrangement is not consistent with the Rietveld-refined occupancies of 0.5(Fe), 0.5(Li) for $12d_2$ and 4*a*, with full occupancies of Fe in $12d_1$ and Li in 4*b* [18]. Further, an attempt to calculate this $P4_332$ structure yielded invariably a conductive state with difficult SCF convergence.

The simplest ordered arrangement of $Li_3Fe_5O_8$ consistent with the average disordered $P4_332$ structure from diffraction results can be achieved within the $C222_1$ subgroup. An energy screening of the nearly-degenerate Fe/Li distributions among sites indicated the one reported in Tables 3 and 5 as the most favoured one (Fig. 4). Insertion of additional Li atoms and shift of iron atoms from tetrahedral to octahedral sites, on passing from the $LiFe_5O_8$ to the $Li_3Fe_5O_8$ compound, are clearly shown in Fig. 5. The arrangement of Fe atoms in the $C222_1$ structure of $Li_3Fe_5O_8$ is compatible with both FM and FFM orderings; the corresponding schemes are reported in Table 5. The results of the least-energy optimizations show that, also for $Li_3Fe_5O_8$, the FFM arrangement is the most stable one. However, the $\Delta E = E(\mathrm{FFM}) - E(\mathrm{FM})$ stabilization energy is only 25% of that obtained for $LiFe_5O_8$ (cf. Tables 4 and 5). This means that the ferrimagnetic spin ordering process $5Fe\uparrow \rightarrow 3Fe\uparrow + 2Fe\downarrow$ is energetically more favoured when the chemical environment of spin-up (octahedral) and spin-down (tetrahedral sites) is different, than when it

Table 4
Wyckoff site occupation patterns, calculated lattice constants and energies of the magnetic structures of $LiFe_5O_8$.

	FM $P4_332$	FFM $P4_332$	AFM $C222_1$	Exp. $P4_332$ [18]
Fe↑	$12d_1 + 8c_a$	$12d_1$	$8c_1 + 8c_2 + 4a_1$	
Fe↓		$8c_a$	$8c_5 + 8c_6 + 4b_1$	
Li	4*b*	4*b*	$4a_2 + 4b_2$	
a (Å)	8.478	8.415	11.951	8.331
b			11.911	
c			8.414	
V (Å^3 f.u.$^{-1}$)	152.34	148.97	149.71	143.67
E + 6928 (hartree f.u.$^{-1}$)	−0.01132	−0.05948	−0.05029	
ΔE (eV Fe atom^{-1})	0	−0.262	−0.212	

Table 5
Wyckoff site occupation patterns, calculated lattice constants and energies of the magnetic structures of $Li_3Fe_5O_8$.

	FM $C222_1$	FFM $C222_1$	Exp. $P4_332$ [18]
Fe↑	$8c_1 + 8c_2 + 4a_1 + 4b_1$ $8c_4 + 4a_3 + 4a_4$	$8c_1 + 8c_2 + 4a_1 + 4b_1$	
Fe↓		$8c_4 + 4a_3 + 4a_4$	
Li	$4a_2 + 4b_2$ $8c_3 + 4b_3 + 4b_4$	$4a_2 + 4b_2$ $8c_3 + 4b_3 + 4b_4$	
a (Å)	12.023	12.033	8.389
b	12.011	11.983	
c	8.541	8.526	
V (Å^3 f.u.$^{-1}$)	154.17	153.67	147.60
E + 6943 (hartree f.u.$^{-1}$)	−0.25704	−0.26946	
ΔE (eV Fe atom^{-1})	0	−0.068	

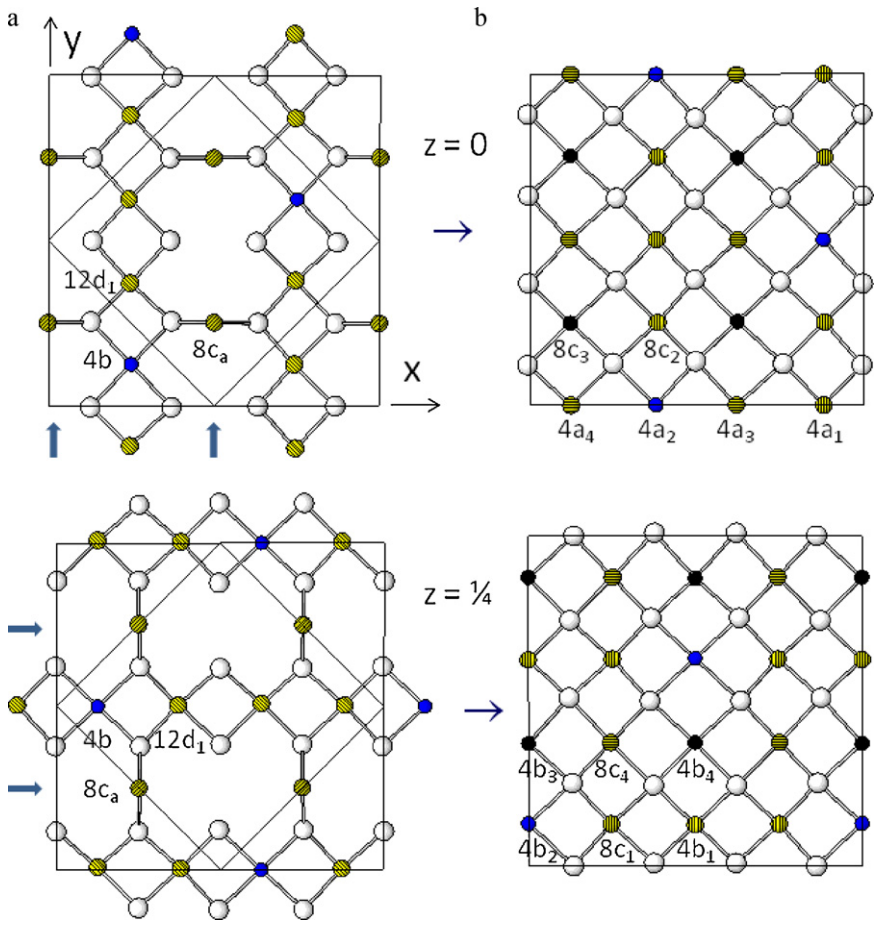

Fig. 5. (0 0 1) atomic layers at $z = 0$ and $z = 1/4$ of (a) $LiFe_5O_8$ and (b) $Li_3Fe_5O_8$ in the $C222_1$ reference frame; in (a) the smaller cubic spinel unit-cell is outlined, too. Cf. Figs. 2 and 4 for notation.

is equal (octahedral sites for both spins). Consequences ensue for the electrochemical reaction (III) energy, as discussed in the next section.

3.3. Energetics of reactions (II) and (III)

The reaction energy of transformation (II) was computed with reference to the $x = 0.25$ case, according to the expression given in Table 6, on the basis of the energies previously discussed for the phases involved. As for Li_2O with antifluorite $Fm\bar{3}m$ structure, the $E = -90.444576$ hartree f.u.$^{-1}$ value (with $a = 4.545$ Å) was obtained and employed. The values of $\Delta_r E$(II) were calculated by combining the energies of the different magnetic states of $LiFe_5O_8$ and $Li_{0.75}FeO_2$ (Tables 1 and 4), to show the effect of magnetic ordering of these compounds on the overall reaction energy, and they are reported in Table 6. The most reliable result (−3.615 eV) corresponds to the FFM-$LiFe_5O_8$/AFM-$Li_{0.75}FeO_2$ case involving the most stable magnetic structures, in agreement also with experimental observation. The computed reaction (II) energy fits in the 4–2 V range of the electrochemical potential measured in the first discharge cycle, though it is slightly larger than the average value.

Similar calculations were performed for reaction (III), on the basis of the total energies obtained for different magnetic arrangements of $LiFe_5O_8$ and $Li_3Fe_5O_8$ (Tables 4 and 5). The results of $\Delta_r E$ are reported in Table 6, and again they appear to be substantially affected by the kind of magnetic ordering assumed. The FFM vs. FM stabilization is much smaller for $Li_3Fe_5O_8$ than for $LiFe_5O_8$, so that the reaction energy is significantly reduced (in absolute value) when both phases are FFM-ordered. Since this is the most stable arrangement, the corresponding $\Delta_r E = -2.096$ eV value should be taken as correct predicted reaction (III) energy. This has to be compared with the average potential of the experimen-

Table 6
Calculated reaction energy (eV Li atom^{-1}) for the two electrochemical reactions supposed to occur in the first discharge (II) and subsequent charge–discharge cycles (III) of the *Pmmn*-$LiFeO_2$ cathode vs. a Li metal anode. Different magnetic orderings of $LiFe_5O_8$, $Li_{0.75}FeO_2$ and $Li_3Fe_5O_8$ are considered.

(II) $4Li_{0.75}FeO_2 + Li \rightarrow (4/5)LiFe_5O_8 + (8/5)Li_2O$; $\Delta_r E = (4/5)E(LiFe_5O_8) - 4E(Li_{0.75}FeO_2) + (8/5)E(Li_2O) - E(Li)$			
$\Delta_r E$ FM–FM	$\Delta_r E$ FFM–FM	$\Delta_r E$ AFM-AFM	$\Delta_r E$ FFM-AFM
−2.780	−3.828	−3.414	−3.615

(III) $(1/2)LiFe_5O_8 + Li \leftrightarrow (1/2)Li_3Fe_5O_8$; $\Delta_r E = (1/2)[E(LiFe_5O_8) - E(LiFe_5O_8)] - E(Li)$	
$\Delta_r E$ FM–FM	$\Delta_r E$ FFM–FFM
−2.583	−2.096

tal charge/discharge curves of *Pmmn*-$LiFeO_2$ in the 1.5–3 V range [8,17], and to those of $LiFe_5O_8$ in the 1.2–3 V [18] or 1.7–3.5 V [19]. The corresponding integral averages are about 2.0, 1.6 and 2.2 V, so that our predicted energy agrees very satisfactorily with the more recent experimental results [8,17,19].

4. Conclusions

A multi-step scheme of electrochemical reactions was proposed to explain charge/discharge voltage and X-ray diffraction data of *Pmmn*-$LiFeO_2$ as positive electrode against a lithium anode. In particular, formation of spinel-like $LiFe_5O_8$, and its subsequent reversible lithiation to a rocksalt-type phase, are the key stages of the process. The third step has also an interest of its own, as it concerns the operation of $LiFe_5O_8$ as starting cathode material. By accurate first-principles calculations, least-energy structural models were determined for the vacancy distribution in defective $Li_{1-x}FeO_2$ and for $Li_3Fe_5O_8$, including various magnetic arrangements. Antiferromagnetic ordering for $Li_{1-x}FeO_2$, and ferrimagnetic ordering for both $LiFe_5O_8$ and $Li_3Fe_5O_8$ are found to characterize the corresponding ground states. The reaction energies at the athermal limit were then computed for all three steps of the process, obtaining values which compare very favourably with the average charge/discharge voltages reported from experiment. This supports strongly the proposed scheme of atomic mechanisms for the 'corrugated layer' lithium iron oxide electrode. First-principles calculations are confirmed to be a valuable aid for interpreting and understanding electrode functionality in batteries.

Acknowledgement

The research was supported by a PRIN grant of MIUR, Rome (Cofin07 Project 200755ZKR3_004).

References

[1] J.W. Fergus, J. Power Sources 195 (2010) 939–954.
[2] B.L. Ellis, K.T. Lee, L.F. Nazar, Chem. Mater. 22 (2010) 691–714.
[3] M. Barré, M. Catti, J. Solid State Chem. 182 (2009) 2549–2554.
[4] M. Tabuchi, K. Ado, H. Sakaebe, C. Masquelier, H. Kageyama, O. Nakamura, Solid State Ionics 79 (1995) 220–226.
[5] A. Meyer, M. Catti, R. Dovesi, J. Phys.: Condens. Matter 22 (2010) 146008/1–146008/8).
[6] N. Douakha, M. Holzapfel, E. Chappel, G. Chouteau, L. Croguennec, A. Ott, B. Ouladdiaf, J. Solid State Chem. 163 (2002) 406–411.
[7] T. Matsumura, R. Kanno, Y. Inaba, Y. Kawamoto, M. Takano, J. Electrochem. Soc. 149 (2002) A1509–A1513.
[8] R. Kanno, T. Shirane, Y. Kawamoto, Y. Takeda, M. Takano, M. Ohashi, Y. Yamaguchi, J. Electrochem. Soc. 143 (1996) 2435–2442.
[9] A.R. Armstrong, D.W. Tee, F. La Mantia, P. Novak, P.G. Bruce, J. Am. Chem. Soc. 130 (2008) 3554–3559.
[10] Y. Sakurai, H. Arai, S. Okada, J. Yamaki, J. Power Sources 68 (1997) 711–715.
[11] P.P. Prosini, M. Carewska, S. Loreti, C. Minarini, S. Passerini, Int. J. Inorg. Mater. 2 (2000) 365–370.
[12] S.-H. Wu, H.-Y. Liu, J. Power Sources 174 (2007) 789–794.
[13] F. Martin, E. Navarrete, J. Morales, C. Roldán, J.R. Ramos-Barrado, L. Sánchez, J. Mater. Chem. 20 (2010) 2847–2852.
[14] L. Bordet-Le Guenne, P. Deniard, A. Lecerf, P. Biensan, C. Siret, L. Fournès, R. Brec, J. Mater. Chem. 9 (1999) 1127–1134.
[15] Y.S. Lee, C.S. Yoon, Y.K. Sun, K. Kobayakawa, Y. Sato, Electrochem. Commun. 4 (2002) 727–731.
[16] Y.S. Lee, S. Sato, Y.K. Sun, K. Kobayakawa, Y. Sato, J. Power Sources 119–121 (2003) 285–289.
[17] Y.S. Lee, S. Sato, M. Tabuchi, C.S. Yoon, Y.K. Sun, K. Kobayakawa, Y. Sato, Electrochem. Commun. 5 (2003) 549–554.
[18] L.A. de Picciotto, M.M. Thackeray, Mater. Res. Bull. 21 (1986) 583–592.
[19] X. Wang, L. Gao, L. Li, H. Zheng, Z. Zhang, W. Yu, Y. Qian, Nanotechnology 16 (2005) 2677–2680.
[20] A. Van der Ven, M.K. Aydinol, G. Ceder, G. Kresse, J. Hafner, Phys. Rev. B 58 (1998) 2975–2987.
[21] G. Ceder, A. Van der Ven, Electrochim. Acta 45 (1999) 131–150.
[22] M. Catti, Phys. Rev. B 61 (2000) 1795–1803.
[23] C.Y. Ouyang, S.Q. Shi, Q. Fang, M.S. Lei, J. Power Sources 175 (2008) 891–896.
[24] S. Laubach, S. Laubach, P.C. Schmidt, D. Ensling, S. Schmid, W. Jaegermann, A. Thißen, K. Nikolowski, H. Eherenberg, Phys. Chem. Chem. Phys. 11 (2009) 3278–3289.
[25] R. Dovesi, V.R. Saunders, C. Roetti, R. Orlando, C.M. Zicovich-Wilson, F. Pascale, B. Civalleri, K. Doll, N.M. Harrison, I.J. Bush, Ph. D'Arco, M. Llunell, CRYSTAL09: User's Manual, University of Torino, Italy, 2009.
[26] C. Lee, W. Yang, R.G. Parr, Phys. Rev. B 37 (1988) 785.
[27] A.D. Becke, J. Chem. Phys. 98 (1993) 5648.
[28] S.J. Marin, M. O'Keeffe, D.E. Partin, J. Solid State Chem. 113 (1994) 413–419.
[29] G.O. White, C.E. Patton, J. Magn. Magn. Mater. 9 (1978) 299–317.
[30] H. Yang, F. Wu, L. Song, M. Zhao, J. Wang, H. Luo, J. Magn. Magn. Mater. 134 (1994) 134–136.
[31] S.Y. An, I.-B. Shim, C.S. Kim, J. Magn. Magn. Mater. 290–291 (2005) 1551–1554.